Space Weather

RESEARCH ARTICLE
10.1029/2022SW003051

Key Points:

- We perform ensemble simulations of radiation belt electron flux decay with a dynamically changing environment at a high time resolution
- Uncertainties in wave amplitude dominantly cause simulation errors, compared to density, wave peak frequency, and background magnetic field
- The magnitude of simulation errors increases with decreasing probability density where the number of ensemble members is large

Supporting Information:

Supporting Information may be found in the online version of this article.

Correspondence to:

M. Hua,
manhua@ucla.edu

Citation:

Hua, M., Bortnik, J., Kellerman, A. C., Camporeale, E., & Ma, Q. (2022). Ensemble modeling of radiation belt electron flux decay following a geomagnetic storm: Dependence on key input parameters. *Space Weather*, *20*, e2022SW003051. https://doi.org/10.1029/2022SW003051

Received 2 FEB 2022
Accepted 1 JUN 2022

Ensemble Modeling of Radiation Belt Electron Flux Decay Following a Geomagnetic Storm: Dependence on Key Input Parameters

Man Hua[1], Jacob Bortnik[1], Adam C. Kellerman[2], Enrico Camporeale[3], and Qianli Ma[1,4]

[1]Department of Atmospheric and Oceanic Sciences, UCLA, Los Angeles, CA, USA, [2]Department of Earth, Planetary, and Space Sciences, UCLA, Los Angeles, CA, USA, [3]CIRES, University of Colorado, Boulder, CO, USA, [4]Center for Space Physics, Boston University, Boston, MA, USA

Abstract We perform an ensemble of quasi-linear diffusion simulations of the radiation belt electron flux decay for ~6 days at L = 3.5 during the recovery phase of the storm on 7 November 2015, where plasmaspheric hiss dominantly drives the electron flux decay process. Based on Van Allen Probes measurements, we use percentiles to sample distributions of the four key input parameters, which are the hiss wave amplitude B_w, hiss wave peak frequency f_m, background magnetic field B_0, and electron density N_e, with 11 points representing that range of each input, leading to 11^4 (~14,600) ensemble members. By developing a Lookup Table method to rapidly calculate the time-dependent diffusion coefficients, the changing wave environment at every time step is incorporated into our ensemble simulations. The comparison between the ensemble simulations and observations reveals the influence of uncertainties in the input parameters on the simulated electron fluxes. Our results demonstrate that the perturbations in B_w are the primary contributors for discrepancies between modeled and observed electron fluxes, while the simulation errors caused by variations in f_m and N_e are strongly energy-dependent. The simulated electron flux using the wave parameters observed at the 50th percentile agrees with observations, and most of the simulation errors increase with decreasing observational probability density of the parameters, with the largest log accuracy ratio of ~14. Our physics-based ensemble modeling provides the essential information about the robustness of radiation belt simulation and forecast considering the uncertainties in the plasma wave measurement or parameterization.

Plain Language Summary Ensemble modeling is a frontier method in the space weather community that can help us understand how uncertainty propagates in the model, which is a necessary step toward both model verification, uncertainty quantification, and assessing the accuracy of forecasts. Based on a typical radiation belt event where plasmaspheric hiss dominantly drives electron flux decay during the recovery phase of a storm, we perform ensemble quasi-linear diffusion simulations of radiation belt electrons to investigate the influence of uncertainties in the four key input parameters on the simulated results. The distributions of input parameters are sampled from Van Allen Probes measurements. By comparing the ensemble simulations with observed electron flux evolutions and calculating the simulation errors, we quantitatively analyze how the uncertainties in the input parameters propagate in the simulations. In addition, using the ensemble technique allows us to turn the physics-based deterministic model into a probabilistic problem. The calculations of the probability density of simulation errors in our ensemble provide useful information that can benefit radiation belt nowcasts and forecasts. Quantifying the uncertainty in our quasi-linear diffusion simulations is a necessary step toward robust radiation belt electron model verification and forecasting.

1. Introduction

Understanding the dynamics and the underlying physical mechanisms of the Earth's radiation belt electron fluxes is important for both nowcasting and forecasting in space weather. Significant advances have been made in understanding radiation belt electron dynamics using both physics-based models (e.g., Beutier & Boscher, 1995; Glauert et al., 2014; Li et al., 2016; Ma et al., 2018, 2015; Reeves et al., 2012; Subbotin & Shprits, 2009; Thorne, Li, et al., 2013; Tu et al., 2013) and machine learning techniques (e.g., Bortnik et al., 2018, 2016; Chu et al., 2021, 2017; Claudepierre & O'Brien, 2020; Pires de Lima et al., 2020; Sarma et al., 2020). It has been well acknowledged that wave-particle interactions play an important role in altering the electron flux distributions

(e.g., Li & Hudson, 2019 and references therein; Thorne, 2010 and references therein). Plasmaspheric hiss is one of the most important drivers of persistent energetic electron loss following injections in the plasmasphere and plumes (e.g., Li et al., 2019; Thorne et al., 2013a; Zhao et al., 2019), which is primarily responsible for the formation of the slot region (e.g., Lyons & Thorne, 1973). The hiss waves could cause significant energetic electron precipitations in the Earth's ionosphere and affect the magnetosphere-ionosphere coupling processes (e.g., Ma et al., 2021). The quasi-linear theory is the most widely adopted methodology to investigate these wave-particle interactions on a global scale, where the scattering and acceleration effects of different wave modes are incorporated as various diffusion coefficients (Schulz & Lanzerotti, 1974). By numerically solving the Fokker-Planck diffusion equation for radiation, the evolution of the electron phase space density can be obtained (e.g., Hua et al., 2020; Ma et al., 2015; Ni et al., 2017; Shprits et al., 2008; Thorne, Li, et al., 2013b; Tu et al., 2014; Xiao et al., 2009). However, the results of diffusion simulations can vary significantly depending on the adopted key input parameters associated with the plasma wave models, background magnetic field model, and electron density model (e.g., Abel & Thorne, 1998; Albert et al., 2020; Camporeale et al., 2016; Hua et al., 2019; Lei et al., 2017; Tu et al., 2013), whose measurements can be insufficient due to limited spatiotemporal coverage of the satellite trajectory, or inaccurate due to the instrument limitation or during extreme events. Accurately modeling the radiation belt electron flux decay and energetic electron precipitation is an important element for space weather nowcasting and forecasting. Therefore, it is important to quantify how the uncertainties of the key parameters due to limited or inaccurate satellite measurements affect radiation belt simulation performance, which helps to predict the radiation belt electron fluxes and their precipitation in the Earth's upper atmosphere.

Owing to the continuous accumulation of high-quality wave and particle measurements from multiple satellite missions and the development of the state-of-art modeling, rapid progress has been made in radiation belt electron forecasting using frontier methods, such as data assimilation, machine learning, and ensemble technique, in the past few decades (e.g., Camporeale, 2019; Camporeale et al., 2018, 2016; Castillo Tibocha et al., 2021; Cervantes et al., 2020; Kellerman, 2018; Kellerman et al., 2014, 2013; Morley et al., 2016; Myagkova et al., 2020; Saikin et al., 2021; Shprits et al., 2013; Smirnov et al., 2020). It is essential to understand how the errors in the model output can be apportioned to the uncertainties in the model input to enhance the model and forecast accuracy (e.g., Horne et al., 2021; Knipp et al., 2018; Morley, 2020). The current study investigates the impact on radiation belt simulations of uncertainties of an event-based wave and plasma models relying on measurements from Van Allen Probes within a limited spatiotemporal coverage during ∼6 days. By sampling input parameters and running a deterministic model numerous times, ensemble simulations can help us understand how the uncertainty propagates in the model, as well as the confidence and range of predicted model outcomes, which is a necessary step toward robust space weather prediction (Murray, 2018). The ensemble modeling technique has gained popularity in space weather forecasting in recent years (e.g., Henley & Pope, 2017; Knipp, 2016 and references therein). For example, ensemble modeling of a coronal mass ejection evaluates the sensitivity of simulations to the model input parameters, which is important for potential model improvements and better predictions (e.g., Barnard et al., 2020; Cash et al., 2015). Chen et al. (2018) used the ensemble approach to investigate the sensitivity of ring current simulations to uncertainties in electric field boundary conditions. Guerra et al. (2020) used ensemble forecasts to improve the predictions of major solar flares by linearly combining multiple existing models.

Camporeale et al. (2016) reported on the first study to investigate the effects of uncertainties in the input parameters on the output of the quasi-linear diffusion simulations using the VERB (Versatile Electron Radiation Belt) code (Subbotin & Shprits, 2009), interpreting the deterministic physics-based model in a probabilistic way. Specifically, they varied the geomagnetic Kp index, the maximum latitude extent of chorus waves, and the electron density in the ensemble simulation with 225 members in total. Based on a sensitivity analysis, they found that perturbations in electron density are primarily responsible for the largest spread in simulated electron fluxes under the impact of chorus waves. However, they used the assumption of Gaussian distributions to sample the distributions of input parameters for simplicity. In addition, they did not include the cross-term diffusion in the simulations nor did they compare the simulated results with observations. Therefore, the effects of model uncertainties due to variations in the input parameters on the radiation belt electron simulations are still only understood in a limited way.

In this paper, we perform an ensemble of quasi-linear diffusion simulations of an outer radiation belt electron flux decay event at L = 3.5 under the impact of plasmaspheric hiss during the recovery phase of the geomagnetic storm on 7 November 2015, which has been previously reported by Ma et al. (2016). As plasmaspheric hiss

plays a dominant role in driving the energetic electron flux evolution in this case (Ma et al., 2016), we limit our analysis to the following four input parameters: (a) hiss wave amplitude (B_w), (b) hiss wave peak frequency (f_m), (c) background magnetic field (B_0), and (d) total electron density (N_e). Based on observations from Van Allen Probes (Mauk et al., 2013), we use nonparametric statistics (i.e., percentiles) to sample the distributions of these four key input parameters with 11 points for each input, leading to 11^4–14,600 ensemble members. We additionally improve the present radiation belt electron diffusion model by incorporating a changing wave environment at every time step in the calculation of the diffusion coefficients by using a rapid Lookup Table (LUT) method. Based on ensemble simulations, we intend to quantify the effects of uncertainties in the input parameters on the simulated electron fluxes, which is crucial for verification and uncertainty quantification of the existing radiation belt model, thereby improving radiation belt forecasts.

The paper is organized as follows. Section 2 presents how we sample the distributions of key input parameters based on Van Allen Probes observations and details about the model of ensemble simulations. In Section 3, we comprehensively analyze our ensemble simulations to see how uncertainties in the input parameters influence the electron flux evolutions and their relative importance to the simulation errors. The conclusions and discussions are presented in Section 4.

2. Data Sample and Model Description

2.1. Sampling Input Parameters Based on Van Allen Probes Observations

Figure 1 presents the sampling distributions of the four input parameters based on both Van Allen Probes observations following the geomagnetic storm on 7 November 2015. As discussed below, we adopt a hiss wave model based on statistics from Li et al. (2015), which is sorted into various geomagnetic conditions according to AL* (where AL* is the minimum AL in the previous 3 hr), as presented in Figure 1a. The background magnetic field (B_0) is observed by the Electric and Magnetic Field Instrument Suite and Integrated Science (EMFISIS; Kletzing et al., 2013) instrument and projected to the geomagnetic equator at L = 3.5 using a dipolar latitudinal variation. In this study, we adopted the McIlwain L values calculated based on the TS04D magnetic field model (Tsyganenko & Sitnov, 2005). The equatorial magnetic fields agree with the dipolar geomagnetic field in general with only small relative deviations (Figure 1b). In contrast, the observed total electron density (N_e) shows strong variation compared with the empirical models from Sheeley et al. (2001) and Ozhogin et al. (2012). We assume the satellite is outside the plasmapause when the in situ density is smaller than either 30 cm^{-3} or the value from the plasma trough density model of Sheeley et al. (2001) or when electron cyclotron harmonic (ECH) waves are observed by the High Frequency Receiver (HFR) onboard EMFISIS (Meredith et al., 2009); otherwise, it is considered to be inside the plasmasphere. The identified plasmapause location along the Van Allen Probes trajectory is shown in Figure 1d. Consistent with the study of Ma et al. (2016), the Van Allen Probes were located mostly outside the plasmapause when crossing L = 3.5 during the first 25 hr and were mostly inside the plasmapause subsequently. However, Van Allen Probes only provided measurements on the dayside (MLT = ∼10 on the outbound trajectory and MLT = ∼17 on the inbound trajectory) during this event. Using THEMIS (Angelopoulos, 2008) measurements on the nightside, Ma et al. (2016) confirmed that the plasmapause locations were higher than L = 3.5 on the nightside in this case. The plasmaspheric hiss wave power is selected with frequencies between 20 and 4,000 Hz and an ellipticity larger than 0.7 (e.g., Li et al., 2015). The integral wave amplitude of plasmaspheric hiss from EMFISIS measurements when the satellites were inside the plasmasphere is presented in Figure 1e. The statistical hiss wave amplitude as a function of MLT based on the observed AL* index (Figure 1a) is displayed in Figure 1f, where we assume the wave amplitude to be zero on the dayside when the observed plasmapause location is smaller than L = 3.5 (since plasmaspheric hiss is confined to the plasmasphere). Due to the limited spatial coverage of the Van Allen Probe measurements on the dayside during this ∼6-day event, we adopt the statistical distribution of wave amplitude from Li et al. (2015) and scale it based on the observed values. It is important to note that the instantaneous spatial extent of the hiss active region is usually less than 3 hr in MLT and less than ∼1 R_E in radial scale (Agapitov et al., 2018, 2021), and the temporal extent is up to ∼10 min at L < ∼4.5 (Zhang et al., 2021), though the correlation scale of hiss waves can indeed extend to a larger MLT sector spanning the dayside (Breneman et al., 2015; Li et al., 2017). Although the limited spatial (L, MLT, and MLAT) and temporal coverage of Van Allen Probes during this event precludes a reliable rescaling of hiss wave amplitude on a global scale, the present study assesses the impact of the uncertainties of the event-based wave and plasma models from such realistic and limited satellite measurements on the radiation belt simulations. For the same reason, we use

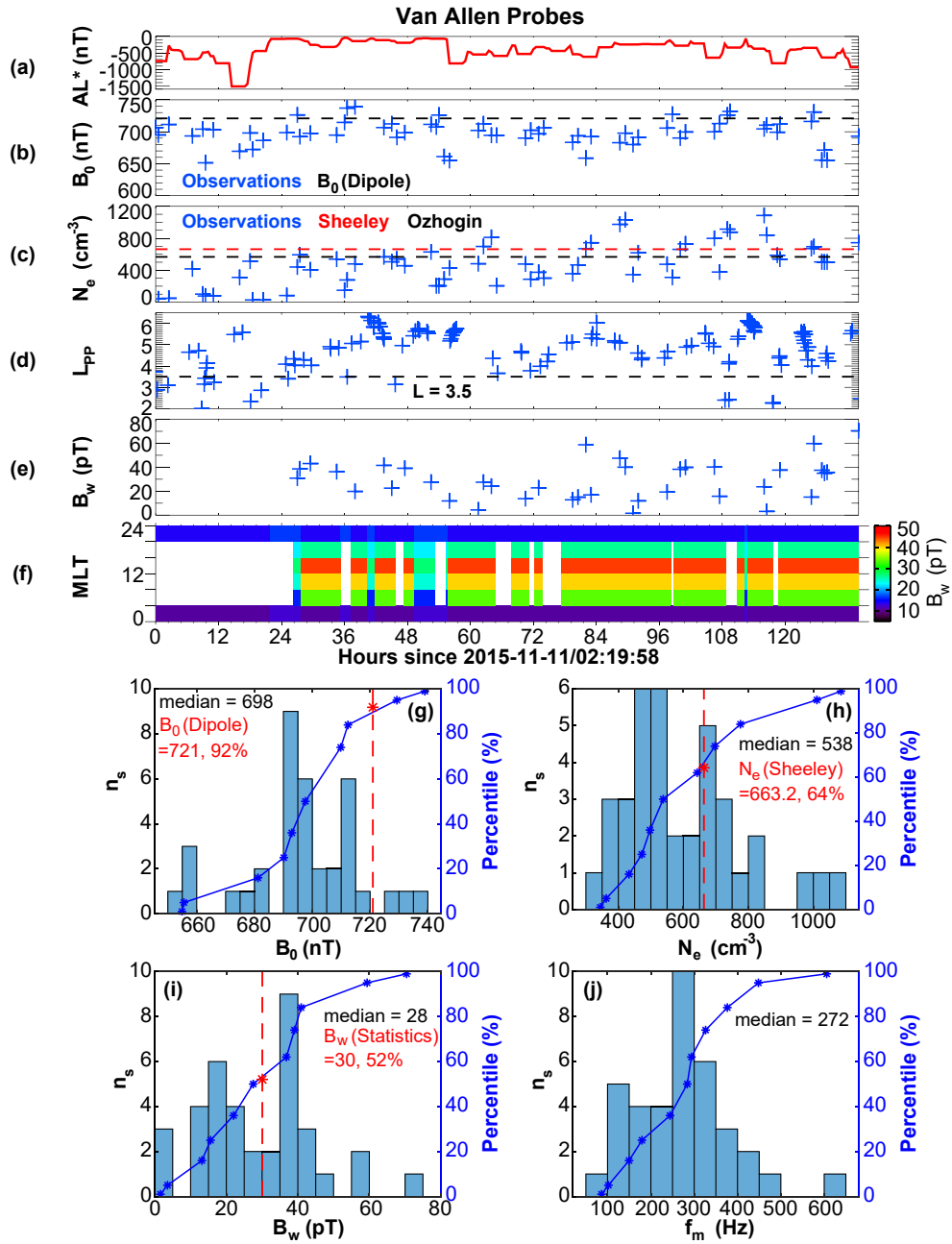

Figure 1. Sampling distributions of input parameters based on Van Allen Probes observations. (a) AL* index, where AL* is the minimum AL in the previous 3 hr. (b) Observed background magnetic field by EMFISIS at L = 3.5 projected to the geomagnetic equator, with the black dashed line representing the dipolar geomagnetic field. (c) Observed electron density (N_e) at L = 3.5 measured by EMFISIS. Here, red and black dashed lines represent the electron density from the empirical models of Sheeley et al. (2001) and Ozhogin et al. (2012), respectively. (d) Plasmapause locations identified from Van Allen Probe observations, with the black dashed line marking L = 3.5. Wave amplitude (B_w) of plasmaspheric hiss at L = 3.5 based on (e) EMFISIS measurements and (f) statistics of Li et al. (2015). Histogram of observed (g) background magnetic field, (h) electron density, (i) wave amplitude, and (j) wave peak frequency of plasmaspheric hiss, with blue star lines representing the sampled input parameter distributions using percentiles. The values from empirical models with corresponding percentiles based on observations are marked by red vertical dashed lines and stars.

the statistical wave frequency spectral shape in different MLT sectors from Li et al. (2015) and shift it to a lower or higher frequency based on the observed wave peak frequency. Note that the shifted wave frequency spectra are still constrained within 20–4,000 Hz and normalized to 10 pT as the diffusion coefficients are proportional to the

square of the wave amplitude in the quasi-linear regime, which allows us to only vary the wave peak frequency with the wave amplitude unchanged.

The histograms of the observed quantities, that is, background magnetic field, electron density, hiss wave amplitude, and hiss wave peak frequency are shown in Figures 1g–1j, with the blue star lines representing the sampled input parameter distributions using percentiles. Specifically, there are 11 levels selected for each input, corresponding to the percentiles of 1%, 5%, 16%, 25%, 36%, 50%, 62%, 74%, 84%, 95%, and 99%, leading to 11^4 members in our ensemble. We use the dipolar geomagnetic field model and assume the electron density does not vary with latitude. Following previous studies (e.g., Hua et al., 2019, 2020), we adopt a latitudinally varying wave normal angle distribution for plasmaspheric hiss at magnetic latitudes ranging from the equator to 45° (Ni et al., 2013).

2.2. Lookup Table Method

In the majority of previous studies, the UCLA Full Diffusion Code (FDC) was used to calculate the wave-induced electron diffusion coefficients (e.g., Ni et al., 2008), where only single point in situ measurements or the statistical values of input parameters related to the wave model, background magnetic field, and electron density were used. It typically takes several hours to calculate diffusion coefficients for a single wave type at one L-shell and one MLT sector. Consequently, it is difficult to incorporate the dynamically changing wave environment at every time step using the FDC method since it is so computationally expensive. The studies of Mourenas and Ripoll (2012) and Artemyev et al. (2013) developed analytical formulas of electron diffusion coefficients scaled with parameters related to the wave models and the total electron density model. In the present study, we develop a Lookup Table (LUT) method (Bortnik et al., 2019), where we use a precalculated diffusion matrix to interpolate the time-dependent diffusion coefficients at every time step. It takes less than 1 s to calculate the diffusion coefficients using the LUT method, which allows us to incorporate the changing wave environment at every time step in our ensemble radiation belt electron simulations. The calculation considers all possible wave-particle resonant interactions for the given wave frequency spectrum, wave normal angle distribution, and latitudinal distribution.

We precompute a large data set of diffusion coefficients using FDC as a function of electron pitch angle and energy, for different wave frequency ranges, latitude ranges, wave normal angle distributions, and f_{pe}/f_{ce} ratios (ratio between the plasma frequency and the electron gyrofrequency). Sufficient calculation resolution is required, because the resonance between an electron (pitch angle α and energy E) and a wave (frequency ω and normal angle θ) may only occur at a specific latitude, and not others. The detailed information about precalculation and the validation of the LUT method is provided in the Supporting Information (Text S1 and Figures S1-S3 in Supporting Information S1). The final diffusion coefficients with a realistic frequency range, latitude range, and normal angle distribution could be constructed as the sum of the precalculated coefficients in each fine frequency range, latitude range, and normal angle distribution, weighted by the wave power at each frequency.

2.3. Two-Dimensional Radiation Belt Model

We simulate the electron flux evolution over a period of 134 hr (~5.6 days) at L = 3.5 at the energy range of 50 keV–5 MeV under the impact of plasmaspheric hiss by numerically solving the two-dimensional Fokker-Planck diffusion equation (e.g., Xiao et al., 2009). The electron phase space density (PSD, f) is related to the differential flux as $f = j/p^2$, where p is the electron momentum. The initial electron PSD distribution is collected by the Energetic Particle, Composition, and Thermal Plasma (ECT) suite (Spence et al., 2013) using the measurements from Magnetic Electron Ion Spectrometer (MagEIS) (Blake et al., 2013), and Relativistic Electron-Proton Telescope (REPT) (Baker et al., 2013) instruments onboard Van Allen Probe A at ~02:20 UT on 11 November 2015 when the satellite was near the geomagnetic equator (|MLAT| < 5°). Van Allen Probes measurements are used to update the electron PSDs at the lower energy boundary. Due to the fact that the observed electron PSDs at ~5 MeV show only small variations, we believe that it is reasonable to approximate the electron PSDs at the upper energy boundary to be constant. We take $f = 0$ inside the bounce loss cone, and $D_{\alpha\alpha}\,(\partial f/\partial\alpha) + D_{\alpha p}\,(\partial f/\partial p) = 0$ at $\alpha = 90°$ (e.g., Albert et al., 2016; Hua et al., 2020), where α is the equatorial pitch angle. Using the LUT method described above, the changing four key input parameters are updated every time whenever the measurements are available or AL* is updated in our ensemble simulations. Note that the time resolution of AL* in the current study is 30 min. Since the present study focuses on the electron flux decay driven by local wave-particle interactions,

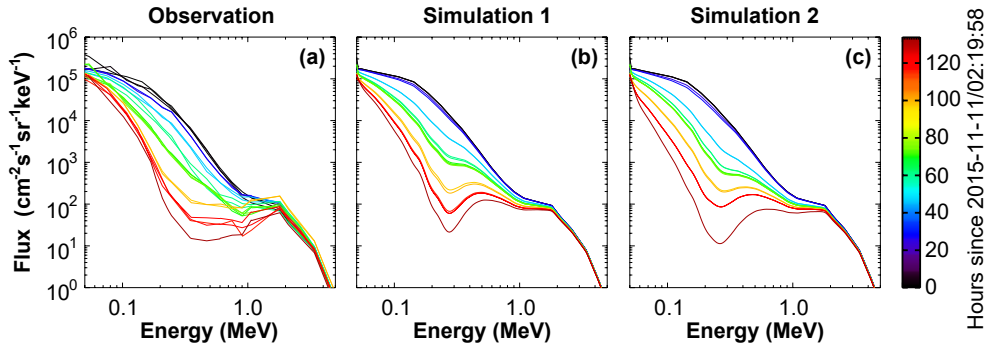

Figure 2. The comparison of spin-averaged electron flux evolutions as a function of energy at color-coded times at $L = 3.5$ from (a) observation, (b) simulation where the 50th percentiles of all input parameters are adopted, and (c) simulation where all input parameters evolving with time based on observations are adopted.

and the typical timescale of radial diffusion at L = 3.5 during a nondisturbed period inside the plasmasphere is larger than 6 days (e.g., Brautigam & Albert, 2000; O'Brien et al., 2016), radial diffusion is not included in our ensemble simulations.

3. Ensemble Simulations

3.1. Simulation Baseline

Figure 2 presents a comparison of the spin-averaged electron flux evolution as a function of energy at color-coded times at L = 3.5 from both observation (Figure 2a) and simulation (Figure 2b) where the 50th percentiles of all four input parameters are adopted (hereafter referred to as simulation 1). The bounce-averaged diffusion coefficients based on these parameters are shown in Figure S2 in Supporting Information S1. The observed electron fluxes are collected from both Van Allen Probes near the geomagnetic equator (|MLAT| < 5°). The overall agreement between the observed and simulated gradual electron flux decay demonstrates that the pitch-angle scattering by plasmaspheric hiss is primarily responsible for the electron flux decay at energies ranging from ~100 to ~900 keV, with the most significant decay around ~300 keV at L = 3.5 during the nondisturbed period, consistent with previous studies that plasmaspheric hiss plays a dominant role in forming the slot region (e.g., Lyons & Thorne, 1973). Furthermore, we also perform a simulation where all four input parameters that evolve with time based on observations (shown in Figure 1) are adopted (hereafter referred to as simulation 2), the result of which is displayed in Figure 2c. Although the electron flux decay in simulation two is slightly faster than in simulation 1, the main characteristics of the electron flux decay are consistent with each other and also agree with the observations. Since the current study intends to quantify the effects of uncertainties in each key input parameter on the simulation results, we regard simulation 1 as the baseline in our ensemble for the following uncertainty quantification so that it will be more convenient to separate the impacts of each input parameter.

3.2. Uncertainty Quantification

3.2.1. Varying Only One Input Parameter

To investigate the sensitivity of the simulated electron fluxes to the uncertainties in each of the four input parameters (B_w, B_0, N_e, and f_m), we first vary only one input parameter at a time and keep the other three inputs unchanged at their baseline levels. Figure 3 shows the regression of ensemble simulations by only varying one input parameter while the 50th percentile of other three inputs are adopted, showing the observed electron flux (j_{obs}) versus simulated ones (j_{sim}) color-coded by the percentile of input parameters of (a–d) hiss wave amplitude, (e–h) hiss wave peak frequency, (i-l) background magnetic field, and (m-p) electron density at four energies ranging from 108 to 749 keV. Here, the dot size is proportional to (100%−|a%−50%|), where a% corresponds to the varied percentile of the inputs. Therefore, the results of the simulation baseline with the 50th percentile of all four inputs are shown as the green dots with the largest size. The comparison is shown at 7 time snapshots with the dots on the top right corner and the bottom left corner in each panel corresponding to the initial condition and the end of the simulation (134 hr), respectively. Besides, the plus lines show the results from simulation 2 where all input

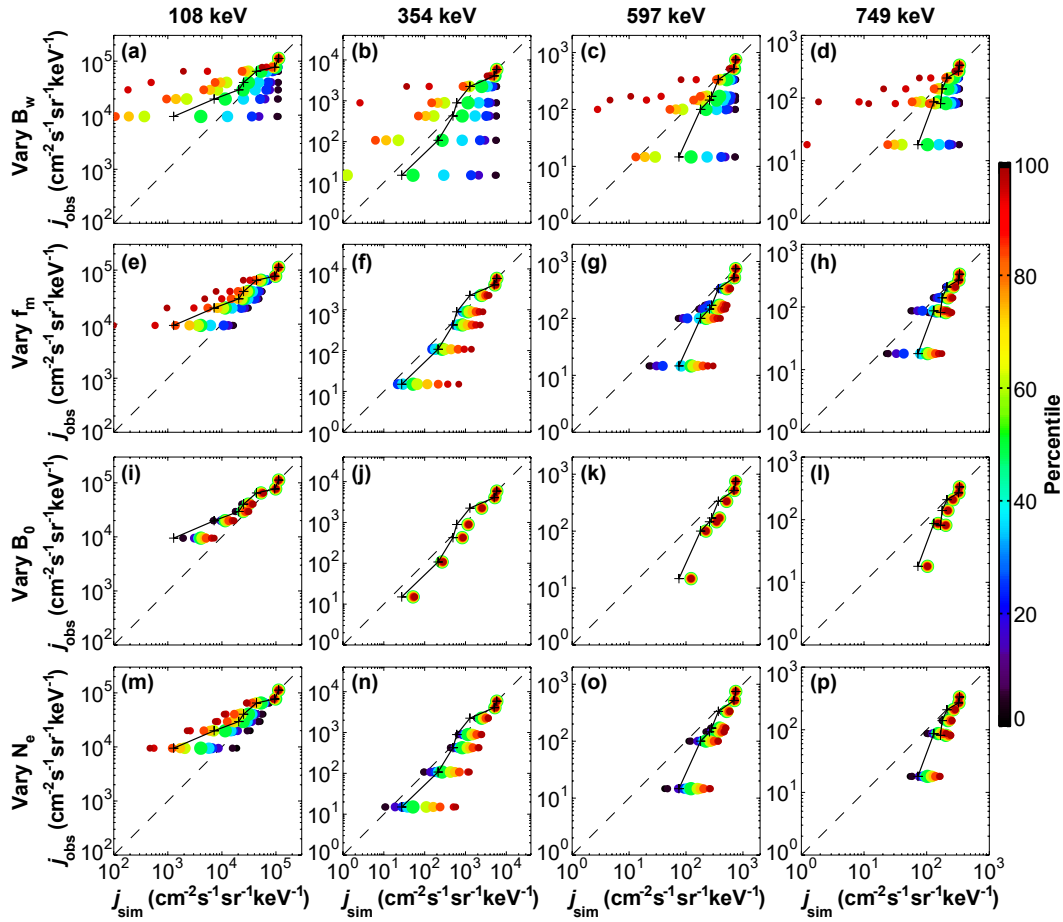

Figure 3. Regression analysis of the ensemble simulations obtained by only varying one input parameter at a time, while the 50th percentiles of the other three inputs are adopted, showing the observed electron flux (j_{obs}) versus simulated ones (j_{sim}) color-coded by the percentile of input parameters of (a–d) hiss wave amplitude, (e–h) hiss wave peak frequency, (i–l) background magnetic field, and (m–p) electron density at indicated four energies. The plus lines correspond to the simulated results where all input parameters evolving with time based on observations are adopted.

parameters that evolve with time based on observations are adopted. The simulated electron fluxes significantly deviate away from the observations when varying the hiss wave amplitude B_w (Figures 1a–1d), demonstrating that B_w plays an important role in causing simulation errors. Specifically, more intense B_w leads to faster decay for all energies (red dots, corresponding to the 99th percentile), while the simulated fluxes barely vary when B_w is too weak to scatter electrons (black dots, corresponding to the first percentile). In contrast, the variation of the simulated electron fluxes shows an opposite trend for lower and higher energy electrons when varying the wave peak frequency f_m and electron density N_e (Figures 1e–1h and 1m–p), which generally enter through the resonance condition. The simulations with larger f_m and N_e result in faster decay at 108 keV but slower decay at higher energies over 354–749 keV compared to the baseline, which is due to the shift of the resonance energies (e.g., Schulz & Lanzerotti, 1974). The uncertainties in the background magnetic field B_0 overall cause the smallest errors in the simulated results (Figures 1i–1l), possibly due to the fact that the relative deviation of the observed B_0 from a dipole model is small.

To quantify the simulation errors, we calculate the simulation errors using the log accuracy ratio of $log_{10}(j_{sim}/j_{obs})$ (e.g., Morley et al., 2016) obtained at the end of the simulations (hereafter referred to as simulation error), which is shown in Figure 4. The simulated electron flux decay is too fast (slow) compared to the observations when the error is smaller (larger) than 0. Clearly, the simulation errors caused by perturbations in B_w are larger than those driven by uncertainties in f_m, N_e, and B_0. Therefore, the influence of the input parameter uncertainties on simulation accuracy follows the sequence of error magnitudes: $Err(B_w) > Err(f_m) \approx Err(N_e) > Err(B_0)$. Note that

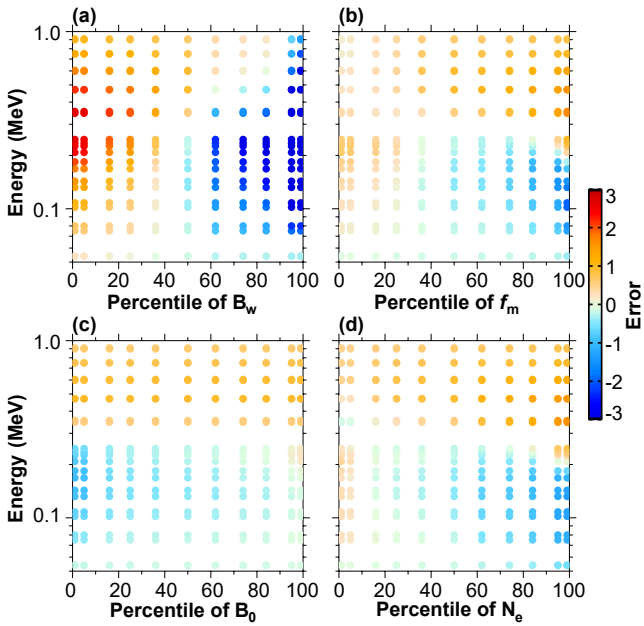

Figure 4. The error of log accuracy ratio at the end of the simulation time period (134 hr) as a function of energy and percentile of (a) hiss wave amplitude, (b) hiss wave peak frequency, (c) background magnetic field, and (d) electron density by only varying one input on the horizontal axis while the 50th percentiles of other three inputs are adopted.

we select the color bar for a symmetric representation of underestimation and overestimation. The simulation errors when varying B_w can be smaller than −3 (Figure 4a), and we discuss the overall largest simulation errors in our ensemble in more detail below.

3.2.2. Varying Two Input Parameters

Figure 5 displays the ensemble simulation errors obtained by varying the two inputs on the vertical axis (percentile of B_w) and horizontal axis (from left to right: percentile of f_m, B_0, and N_e), while the 50th percentile is adopted for the remaining two input parameters. It is interesting to see that the fastest (shown as blue color) and slowest (shown as red color) simulated electron flux decay is always associated with the largest and smallest B_w regardless of the variations in f_m, B_0, and N_e. From the first and the last columns, we can see a similar opposite trend of the errors for lower and higher energies when varying between f_m and N_e, showing that larger f_m and N_e are more favorable for decay at lower energies and vice versa. Therefore, the energy of the most efficient electron flux decay strongly depends on f_m and N_e. The perturbations in B_0 only slightly influence the simulation errors at 108 keV, while they barely affect simulation errors at higher energies, as shown in the second column.

3.2.3. Varying All Input Parameters

The goal of our ensemble simulations is to quantify the extremes of the fastest and slowest decay in our ensemble simulations. Therefore, for each point in B_w at a given energy, we calculate the smallest (corresponding to the fastest decay) and largest (corresponding to the slowest decay) simulation errors when varying the other three inputs and find the corresponding percentiles of the other three inputs, as shown in Figure 6. Overall, the largest errors of the fastest and slowest simulated electron flux decays are found for extreme cases of these four inputs, associated with the largest B_w and smallest B_0, respectively. Due to the fact that the variation of B_0 plays an insignificant role in affecting simulated results at higher energies (>108 keV) as mentioned above, the percentiles of B_0 associated with the fastest and slowest decay do not show a clear trend. The absolute value of the errors of the fastest decay can reach ∼10 for electrons over 108–597 keV energies, which is much larger than the errors of the slowest decay (<5). The largest error of the slowest decay is the flux ratio between the initial condition and the observed fluxes at the end of the simulation, as the smallest B_w is too weak to scatter the electrons.

Based on our ensemble, we can turn the physics-based deterministic model into a probabilistic problem. We further calculate the probability density of the simulation errors in our ensemble to provide more useful information that can benefit the nowcast and forecast of the radiation belt electron flux distribution. Here, we calculate the probability density based on the following steps:

1. Based on the observations during this whole event in ∼6 days as shown in Figure 1, we get the probability density function (PDF) of these four key input parameters using the Gaussian fitting $\frac{1}{\sigma\sqrt{2\pi}}\exp\left(-0.5\times\left(\frac{x-\mu}{\sigma}\right)^2\right)$, where x is the value of the input parameters. Here, the mean value (μ) and standard deviation (σ) for each of the four input parameters are given at the top right corner in Figures 7a–7d. The fitting results are shown as the red lines in Figures 7a–7d.
2. We calculate the probability density for each point of the sampled four input parameters by using the Gaussian-fitted PDF, which are shown as red dots in Figures 7a–7d.
3. By assuming the probability density is independent for these four input parameters, the probability density of a member in our ensemble equals to the product of the probability density of each of the four inputs that corresponds to this member. The results of each ensemble member are shown in Figures 7e–7h as dots with the blue and red color showing the overestimation and underestimation of electron flux decay, respectively.
4. We set a probability density grid that is uniformly distributed in logarithmic space from 10^{-15} to 10^{-8} 1/nT/cm^{-3}/pT/Hz with 21 points in total. We calculate the median error of the ensemble members with a probability density that falls into the corresponding bin for Error >0 and Error <0 separately, which are shown as the red

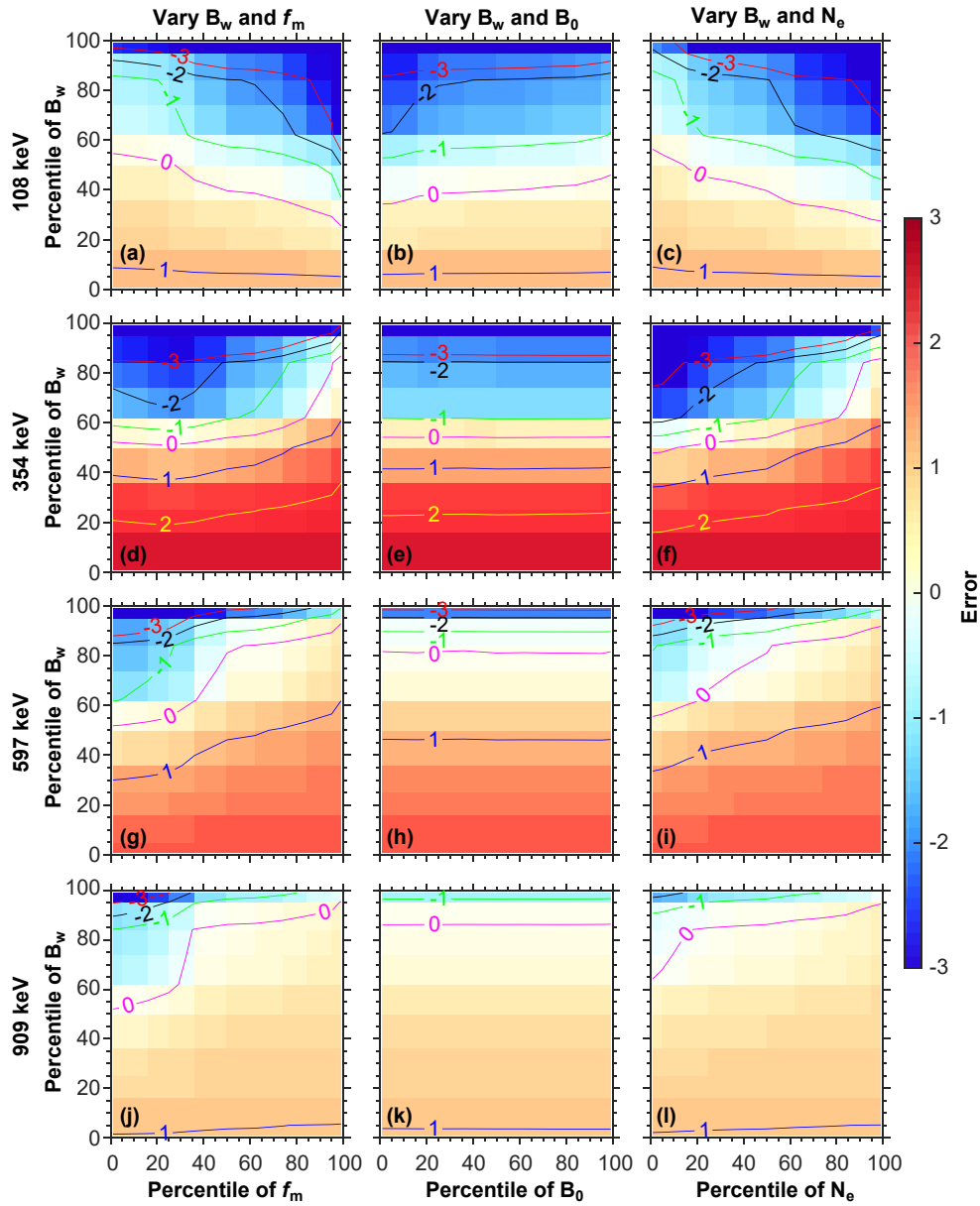

Figure 5. The error of log accuracy ratio at the end of simulations (134 hr) by only varying the two inputs on the vertical axis (percentile of hiss wave amplitude) and horizontal axis (from left to right: percentile of hiss wave peak frequency, background magnetic field, and electron density), while 50th percentile is adopted for the left two input parameters. The color-coded curves represent the contour of the isolines.

and blue circles in Figures 7e–7h. The size of the circle is proportional to log(n_s), where n_s is the number of the ensemble members that fall into the corresponding bin. In addition, the lower and upper quartiles are shown as the error bars below and above each circle.

Figure 7 presents the error of log accuracy ratio of the ensemble simulations versus probability density at 108–749 keV energies. The deviation between simulated electron fluxes and observations for 108 keV electrons becomes more significant with decreasing probability density, because electrons at this energy channel are close to the efficient resonant energy range by plasmaspheric hiss when varying between f_m and N_e. Overall, the magnitude of errors for electrons at higher energies (354–749 keV) increases with decreasing probability density for most of the errors where the number of ensemble members is large. However, there are a few points of errors with small probability density for higher energy electrons, which are caused by the shifting of resonant energy to

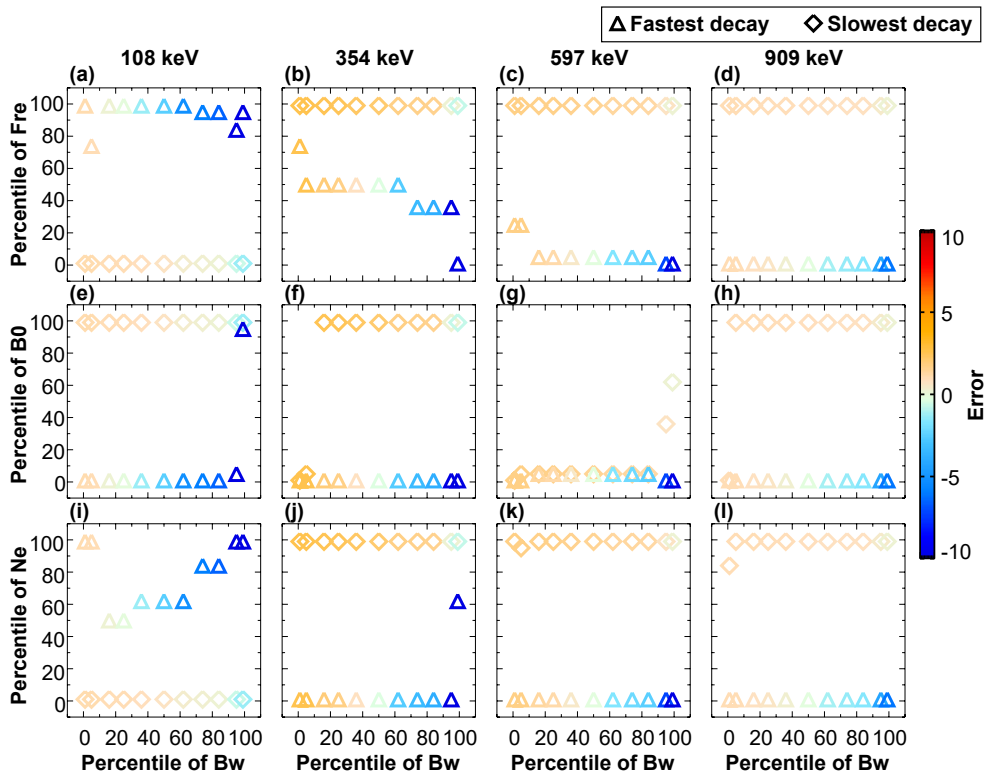

Figure 6. The error of log accuracy ratio of the fastest (triangles) and slowest (diamonds) electron flux decay in the ensemble simulations as a function of percentile of hiss wave amplitude on the horizontal axis and percentile of (a–d) hiss wave peak frequency, (e–h) background magnetic field, and (i–l) electron density on the vertical axis.

lower energies when varying f_m and N_e to the extreme case. The smallest negative errors of the fastest decay in our ensemble can reach about −13 for electrons over 108–597 keV energies, which means that the simulations overestimate the decay by 13 orders of magnitude compared to the observations. For the probability densities of data sampling above 10^{-10} 1/nT/cm^{-3}/pT/Hz, the median error of underestimation is about −2 at 354 keV energy, indicating that the simulated electron flux is 100 times lower than the observation if each of the simulation parameters is not chosen properly. Therefore, the simulations of radiation belt electrons strongly depend on the uncertainties in the key input parameters.

4. Conclusions and Discussions

In the present study, we perform an ensemble of quasi-linear diffusion simulations of radiation belt electron flux decay for ∼6 days during the recovery phase of the storm on 7 November 2015, which is a typical event where wave-particle interactions by plasmaspheric hiss dominantly drive the electron flux decay at L = 3.5. Based on Van Allen Probes measurements during this ∼5-day event, we use nonparametric statistics (percentiles) to sample the distributions of the four key input parameters, including the hiss wave amplitude B_w, hiss wave peak frequency f_m, background magnetic field B_0, and electron density N_e. We develop a Lookup Table (LUT) method to calculate the time-dependent diffusion coefficients, which allows us to incorporate the changing wave environment at every time step in our ensemble simulations. By running ensemble simulations with 11^4 members in total and comparing them with observed electron flux evolutions from Van Allen Probes, we comprehensively and quantitatively analyze the effects of uncertainties in the input parameters on the simulated results. Our principle conclusions are as follows:

1. The uncertainties in hiss wave amplitude play a dominant role in driving the discrepancies between model and observed results and the influence of the input parameter uncertainties on simulation accuracy follows the sequence of errors $Err(B_w) > Err(f_m) \approx Err(N_e) > Err(B_0)$. This result is different from the simulation of electron acceleration due to chorus waves by Camporeale et al. (2016), which demonstrates that the

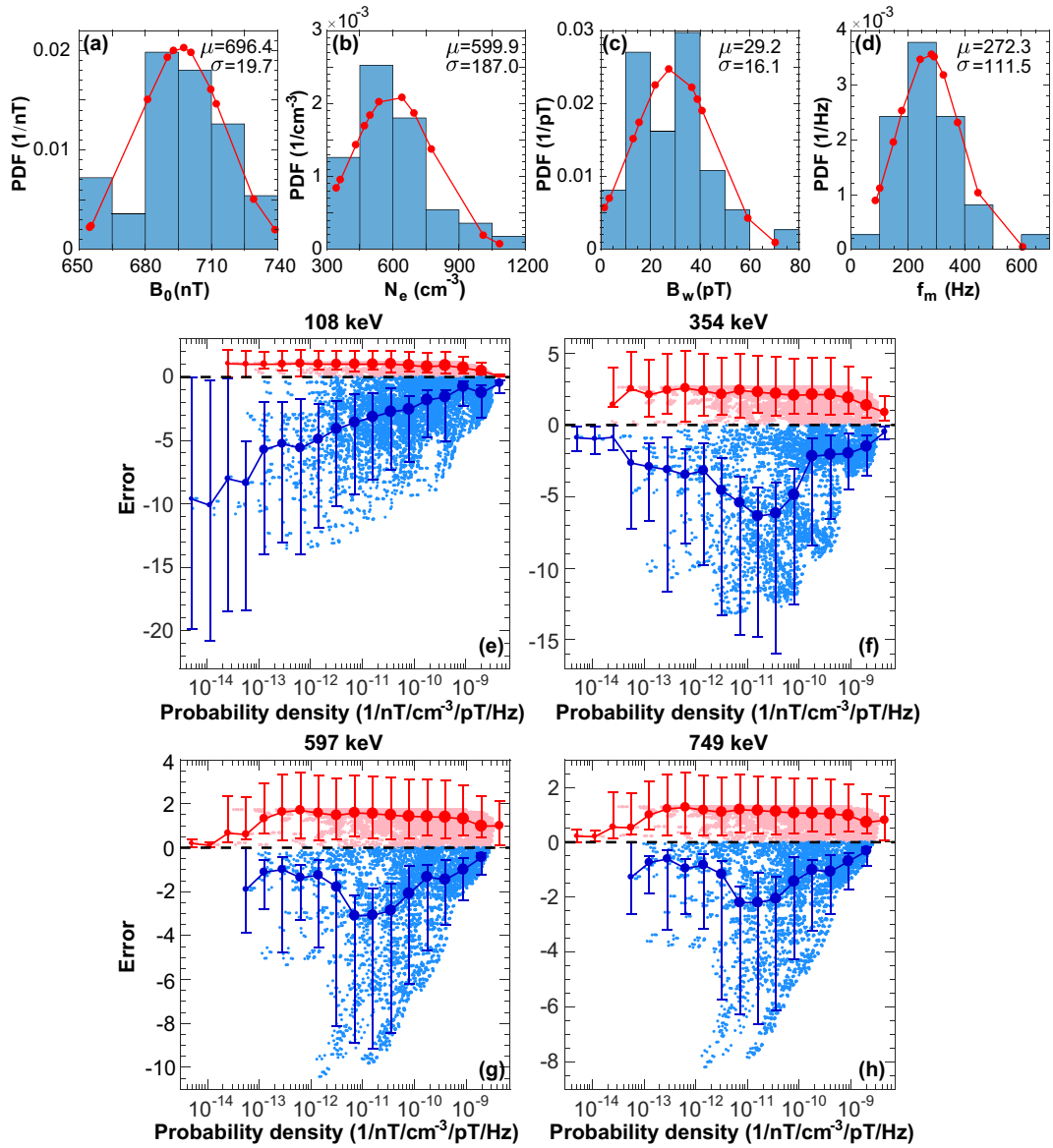

Figure 7. The distribution of probability density function (PDF) of (a) the background magnetic field, (b) the total electron density, (c) the hiss wave amplitude, and (d) the hiss wave peak frequency based on observations. The red lines show the Gaussian fitting of the PDF with the corresponding mean value (μ) and standard deviation (σ) given at the top right corner in each panel. (e)–(h) The error of log accuracy ratio of the ensemble simulations versus probability density at indicated energies, with light blue and light red dots showing the overestimation and underestimation of electron flux decay, respectively. The blue and red dotted lines show the median values, with error bars below and above the dots representing the lower and upper quartiles, respectively.

uncertainties in electron density is primarily responsible for the simulation errors. It is probably due to the fast variation of the hiss wave amplitude in space and limited spatiotemporal satellite coverage during this event, that the event-based inaccuracy in hiss wave amplitude dominantly causes the simulation errors. Furthermore, the analytical estimations of quasi-linear electron diffusion coefficients from studies of Mourenas and Ripoll (2012) and Artemyev et al. (2013) demonstrate the strongest dependence on wave amplitude compared to f_{ce}/f_{pe} or f_{ce}/f_m, which amplifies the impact of uncertainties of wave amplitude on the simulation errors.

2. The perturbations in hiss wave peak frequency and electron density cause an opposite trend of the simulation errors for lower and higher energies due to the shift of the resonance energies, showing that the larger f_m and N_e are more favorable for decay at lower energies and vice versa. Therefore, the energy of the most efficient electron flux decay strongly depends on f_m and N_e.

3. The magnitude of simulation errors increases with decreasing probability density for most of the errors where the number of ensemble members is large, with the largest overestimation of decay reaching 13 orders of magnitude compared to the observations. Therefore, the simulations of radiation belt electrons strongly depend on the uncertainties in the key input parameters.

Although our results contribute to a better understanding of how the inaccuracy in the simulated electron flux evolution is apportioned to event-based uncertainty in the four key input parameters from the realistic and limited satellite measurements, we note some limitations, possible improvements, and future work of the present study. First, the input sampling is based on a limited spatial (i.e., L, MLT, and MLAT) and temporal coverage of Van Allen Probes during this event. The technique of inferring hiss wave amplitude from the electron fluxes measured by Polar Orbiting Environmental Satellites (POES) can help to improve the accuracy of current event-based wave models (de Soria-Santacruz et al., 2015). Second, while the quasi-linear theory is most widely adopted to reproduce the essential features of the observed electron flux dynamics on a global scale, it may underestimate the electron scattering effect by intense coherent plasmaspheric hiss (e.g., Tsurutani et al., 2018). Third, the calculation of the probability density of a member in our ensemble is based on the assumption that the probability density is independent of the four key input parameters, which means that any combination of them is possible in our ensemble simulations. As we use the percentile to sample the event-based distributions of inputs, the values of these four inputs are within an observable range in reality even for the extreme cases. For example, the most intense wave amplitude of hiss (corresponding to the 99th percentile of B_w) is below 80 pT, which can be observed in the high-density region inside the plasmasphere or plumes (e.g., Khazanov & Ma, 2021; Ma et al., 2021). In addition, the extreme cases of electron total density (corresponding to the 1st and 99th percentile of N_e) are within a factor of 2 compared to the empirical model from Sheeley et al. (2001), which still represents the high-density region as the typical density in the plasmatrough is below 50 cm^{-3}. However, there can be correlations among these four inputs in reality. As the current study is limited to the analysis based on a typical event, it is difficult to determine the correlations (or more accurately, the joint probability distribution) among these four input parameters. Analyzing multiple events (such as superposed epoch analysis) that are similar to the current one in terms of geomagnetic conditions and the gradual electron flux decay mainly driven by hiss can help to provide better distributions of all inputs and improve the understanding of the extreme cases. Furthermore, we can estimate the cross-correlation between these inputs based on multiple events analysis, which is computationally challenging and beyond the scope of this study and is left to future work.

In conclusion, our study provides important quantification of how event-based uncertainties in the key input parameters influence the simulated electron flux decay driven by hiss. The calculations of the probability density of the simulation errors in our ensemble enable us to evaluate the dependence of the radiation belt electron lifetime on the key parameters, which can benefit radiation belt nowcast and forecast. Quantifying the uncertainty in our quasi-linear diffusion simulations is a necessary step toward robust verification and confidence estimation of our radiation belt electron hindcast and forecast models.

Data Availability Statement

The EMFISIS data were obtained from http://emfisis.physics.uiowa.edu/Flight/. The ECT data were obtained from https://rbsp-ect.newmexicoconsortium.org/data_pub/. The AL index was obtained from the OMNI data set (https://omniweb.gsfc.nasa.gov/ow_min.html). The results of ensemble simulations and the source data used to produce figures in the present study are publicly available at https://doi.org/10.6084/m9.figshare.19400459 (Hua et al., 2022)

Acknowledgments
We acknowledge the Van Allen Probes mission, particularly the EMFISIS and ECT team for providing the wave and particle data. JB and MH gratefully acknowledge support from subgrant no. 1559841 to the University of California, Los Angeles, from the University of Colorado Boulder under NASA Prime Grant agreement no. 80NSSC20K1580, and NASA/SWO2R Grant No. 80NSSC19K0239. Q. M. would like to acknowledge the NASA Grant No. 80NSSC20K0196. ACK would like to acknowledge support from NASA grants 80NSSC20K1402 and 80NSSC20K1281. EC is partially supported by NASA grants 80NSSC20K1580, 80NSSC20K1275, 80NSSC21K1555.

References

Abel, B., & Thorne, R. M. (1998). Electron scattering loss in earth's inner magnetosphere: 2. Sensitivity to model parameters. *Journal of Geophysical Research*, *103*(A2), 2397–2407. https://doi.org/10.1029/97JA02920

Agapitov, O., Mourenas, D., Artemyev, A., Breneman, A., Bonnell, J. W., Hospodarsky, G., & Wygant, J. (2021). Chorus and hiss scales in the inner magnetosphere: Statistics from high-resolution filter bank (FBK) Van Allen proves multi-point measurements. *Journal of Geophysical Research: Space Physics*, *126*(7), e2020JA028998. https://doi.org/10.1029/2020JA028998

Agapitov, O., Mourenas, D., Artemyev, A., Mozer, F. S., Bonnell, J. W., Angelopoulos, V., et al. (2018). Spatial extent and temporal correlation of chorus and hiss: Statistical results from multipoint THEMIS observations. *Journal of Geophysical Research: Space Physics*, *123*(10), 8317–8330. https://doi.org/10.1029/2018JA025725

Albert, J. M., Starks, M. J., Horne, R. B., Meredith, N. P., & Glauert, S. A. (2016). Quasi-linear simulations of inner radiation belt electron pitch angle and energy distributions. *Geophysical Research Letters*, *43*(6), 2381–2388. https://doi.org/10.1002/2016GL067938

Albert, J. M., Starks, M. J., Selesnick, R. S., Ling, A. G., O'Malley, S., & Quinn, R. A. (2020). VLF transmitters and lightning-generated whistlers: 2. Diffusion of radiation belt electrons. *Journal of Geophysical Research: Space Physics*, *125*(3), e2019JA027030. https://doi.org/10.1029/2019JA027030

Angelopoulos, V. (2008). The THEMIS mission. *Space Science Reviews*, *141*, 5–34. https://doi.org/10.1007/s11214-008-9336-1

Artemyev, A. V., Mourenas, D., Agapitov, O. V., & Krasnoselskikh, V. V. (2013). Parametric validations of analytical lifetime estimates for radiation belt electron diffusion by whistler waves. *Annales Geophysicae*, *31*(4), 599–624. https://doi.org/10.5194/angeo-31-599-2013

Baker, D. N., Kanekal, S. G., Hoxie, V. C., Bastie, S., Bolton, M., Li, X., et al. (2013). The relativistic electron-proton telescope (REPT) instrument on board the radiation belt storm Probes (RBSP) spacecraft: Characterization of Earth's radiation belt high-energy particle populations. *Space Science Reviews*, *179*(1-4), 337–381. https://doi.org/10.1007/s11214-012-9950-9

Barnard, L., Owens, M. J., Scott, C. J., & de Koning, C. A. (2020). Ensemble CME modeling constrained by heliospheric imager observations. *AGU Advances*, *1*(3), e2020AV000214. https://doi.org/10.1029/2020AV000214

Beutier, T., & Boscher, D. (1995). A three-dimensional analysis of the electron radiation belt by the Salammbô code. *Journal of Geophysical Research*, *100*(A8), 14853–14861. https://doi.org/10.1029/94JA03066

Blake, J. B., Carranza, P. A., Claudepierre, S. G., Clemmons, J. H., Crain, W. R., Dotan, Y., et al. (2013). The magnetic electron Ion spectrometer (MagEIS) instruments aboard the radiation belt storm Probe (RBSP) spacecraft. *Space Science Reviews*, *179*(1-4), 383–421. https://doi.org/10.1007/s11214-013-9991-8

Bortnik, J., Chu, X., Ma, Q., Li, W., Zhang, X., Thorne, R. M., et al. (2018). Artificial neural networks for determining magnetospheric conditions. In E. Camporeale, S. Wing, & J. R. Johnson (Eds.), *Machine learning techniques for space weather* (pp. 279–300). Elsevier. https://doi.org/10.1016/b978-0-12-811788-0.00011-1

Bortnik, J., Li, W., Thorne, R. M., & Angelopoulos, V. (2016). A unified approach to inner magnetospheric state prediction. *Journal of Geophysical Research: Space Physics*, *121*(3), 2423–2430. https://doi.org/10.1002/2015ja021733

Bortnik, J., Ma, Q., Chu, X., Li, W., Claudepierre, S. G., Ni, B., & Angelopoulos, V. (2019). The use of machine learning for the rapid prediction of radiation belt dynamics. In *Paper presented at American geophysical union, fall meeting 2019*. Retrieved from https://ui.adsabs.harvard.edu/#abs/2019AGUFMSM52A.02B/abstract

Brautigam, D. H., & Albert, J. M. (2000). Radial diffusion analysis of outer radiation belt electrons during the October 9, 1990, magnetic storm. *Journal of Geophysical Research*, *105*(A1), 291–309. https://doi.org/10.1029/1999JA900344

Breneman, A., Halford, A., Millan, R., McCarthy, M., Fennell, J., Sample, J., et al. (2015). Global-scale coherence modulation of radiation-belt electron loss from plasmaspheric hiss. *Nature*, *523*(7559), 193–195. https://doi.org/10.1038/nature14515

Camporeale, E. (2019). The challenge of machine learning in Space Weather: Nowcasting and forecasting. *Space Weather*, *17*(8), 1166–1207. https://doi.org/10.1029/2018SW002061

Camporeale, E., Shprits, Y., Chandorkar, M., Drozdov, A., & Wing, S. (2016). On the propagation of uncertainties in radiation belt simulations. *Space Weather*, *14*(11), 982–992. https://doi.org/10.1002/2016SW001494

Camporeale, E., Wing, S., & Johnson, J. R. (2018). *Machine learning techniques for space weather*. Elsevier.

Cash, M. D., Biesecker, D. A., Pizzo, V., de Koning, C. A., Millward, G., Arge, C. N., et al. (2015). Ensemble modeling of the 23 july 2012 coronal mass ejection. *Space Weather*, *13*(10), 611–625. https://doi.org/10.1002/2015SW001232

Castillo Tibocha, A. M., de Wiljes, J., Shprits, Y. Y., & Aseev, N. A. (2021). Reconstructing the dynamics of the outer electron radiation belt by means of the standard and ensemble Kalman filter with the VERB-3D code. *Space Weather*, *19*(10), e2020SW002672. https://doi.org/10.1029/2020SW002672

Cervantes, S., Shprits, Y. Y., Aseev, N. A., Drozdov, A. Y., Castillo, A., & Stolle, C. (2020). Identifying radiation belt electron source and loss processes by assimilating spacecraft data in a three-dimensional diffusion model. *Journal of Geophysical Research: Space Physics*, *125*(1), e2019JA027514. https://doi.org/10.1029/2019JA027514

Chen, M. W., O'Brien, T. P., Lemon, C. L., & Guild, T. B. (2018). Effects of uncertainties in electric field boundary conditions for ring current simulations. *Journal of Geophysical Research: Space Physics*, *123*(1), 638–652. https://doi.org/10.1002/2017JA024496

Chu, X., Bortnik, J., Li, W., Ma, Q., Denton, R., Yue, C., et al. (2017). A neural network model of three-dimensional dynamic electron density in the inner magnetosphere. *Journal of Geophysical Research: Space Physics*, *122*(9), 9183–9197. https://doi.org/10.1002/2017ja024464

Chu, X., Ma, D., Bortnik, J., Tobiska, W. K., Cruz, A., Bouwer, S. D., et al. (2021). Relativistic electron model in the outer radiation belt using a neural network approach. *Space Weather*, *19*(12), e2021SW002808. https://doi.org/10.1029/2021SW002808

Claudepierre, S. G., & O'Brien, T. P. (2020). Specifying high-altitude electrons using low-altitude LEO systems: The SHELLS model. *Space Weather*, *18*(3), e2019SW002402. https://doi.org/10.1029/2019SW002402

de Soria-Santacruz, M., Li, W., Thorne, R. M., Ma, Q., Bortnik, J., Ni, B., et al. (2015). Analysis of plasmaspheric hiss wave amplitudes inferred from low-altitude POES electron data: Validation with conjunctive Van Allen Probes observations. *Journal of Geophysical Research: Space Physics*, *120*(10), 8681–8691. https://doi.org/10.1002/2015JA021148

Glauert, S. A., Horne, R. B., & Meredith, N. P. (2014). Three-dimensional electron radiation belt simulations using the BAS Radiation Belt Model with new diffusion models for chorus, plasmaspheric hiss, and lightning-generated whistlers. *Journal of Geophysical Research: Space Physics*, *119*(1), 268–289. https://doi.org/10.1002/2013ja019281

Guerra, J. A., Murray, S. A., Bloomfield, D. S., & Gallagher, P. T. (2020). Ensemble forecasting of major solar flares: Methods for combining models. *Journal of Space Weather and Space Climate*, *10*, 38. https://doi.org/10.1051/swsc/2020042

Henley, E. M., & Pope, E. C. D. (2017). Cost-loss analysis of ensemble solar wind forecasting: Space weather use of terrestrial weather tools. *Space Weather*, *15*(12), 1562–1566. https://doi.org/10.1002/2017SW001758

Horne, R. B., Glauert, S. A., Kirsch, P., Heynderickx, D., Bingham, S., Thorn, P., et al. (2021). The satellite risk prediction and radiation forecast system (SaRIF). *Space Weather*, *19*(12), e2021SW002823. https://doi.org/10.1029/2021SW002823

Hua, M., Bortnik, J., Kellerman, A. C., Camporeale, E., Ma, Q. (2022). Ensemble Modeling of Radiation Belt Electron Flux Decay Following a Geomagnetic Storm: Dependence on Key Input Parameters [Dataset]. https://doi.org/10.6084/m9.figshare.19400459.v2

Hua, M., Li, W., Ni, B., Ma, Q., Green, A., Shen, X.-C., et al. (2020). Very-low-frequency transmitters bifurcate energetic electron belt in near-earth space. *Nature Communications*, *11*(1), 4847. https://doi.org/10.1038/s41467-020-18545-y

Hua, M., Ni, B., Li, W., Gu, X., Fu, S., Shi, R., et al. (2019). Evolution of radiation belt electron pitch angle distribution due to combined scattering by plasmaspheric hiss and magnetosonic waves. *Geophysical Research Letters*, *46*(6), 3033–3042. https://doi.org/10.1029/2018GL081828

Kellerman, A. C. (2018). Prediction of MeV electron fluxes and forecast verification. In E. Camporeale, S. Wing, & J. R. Johnson (Eds.), *Machine learning techniques for space weather* (pp. 259–278). Elsevier. https://doi.org/10.1016/B978-0-12-811788-0.00010-X

Kellerman, A. C., Shprits, Y. Y., Kondrashov, D., Subbotin, D., Makarevich, R. A., Donovan, E., & Nagai, T. (2014). Three-dimensional data assimilation and reanalysis of radiation belt electrons: Observations of a four-zone structure using five spacecraft and the VERB code. *Journal of Geophysical Research: Space Physics*, *119*(11), 8764–8783. https://doi.org/10.1002/2014JA020171

Kellerman, A. C., Shprits, Y. Y., & Turner, D. L. (2013). A geosynchronous radiation–belt electron empirical prediction (GREEP) model. *Space Weather*, *11*(8), 463–475. https://doi.org/10.1002/swe.20074

Khazanov, G. V., & Ma, Q. (2021). Dayside low energy electron precipitation driven by hiss waves in the presence of ionospheric photoelectrons. *Journal of Geophysical Research: Space Physics*, *126*(12), e2021JA030048. https://doi.org/10.1029/2021JA030048

Kletzing, C. A., Kurth, W. S., Acuna, M., MacDowall, R. J., Torbert, R. B., Averkamp, T., et al. (2013). The electric and magnetic field instrument suit and integrated science (EMFISIS) on RBSP. *Space Science Reviews*, *179*(1-4), 127–181. https://doi.org/10.1007/s11214-013-9993-6

Knipp, D. J. (2016). Advances in space weather ensemble forecasting. *Space Weather*, *14*(2), 52–53. https://doi.org/10.1002/2016SW001366

Knipp, D. J., Hapgood, M. A., & Welling, D. (2018). Communicating uncertainty and reliability in space weather data, models, and applications. *Space Weather*, *16*(10), 1453–1454. https://doi.org/10.1029/2018SW002083

Lei, M., Xie, L., Li, J., Pu, Z., Fu, S., Ni, B., et al. (2017). The radiation belt electron scattering by magnetosonic wave: Dependence on key parameters. *Journal of Geophysical Research: Space Physics*, *122*(12), 12338–12352. https://doi.org/10.1002/2016JA023801

Li, J., Bortnik, J., Li, W., Thorne, R. M., Ma, Q., Chu, X., et al. (2017). Coherently modulated whistler mode waves simultaneously observed over unexpectedly large spatial scales. *Journal of Geophysical Research: Space Physics*, *122*(2), 1871–1882. https://doi.org/10.1002/2016JA023706

Li, W., & Hudson, M. K. (2019). Earth's van allen radiation belts: From discovery to the van allen Probes era. *Journal of Geophysical Research: Space Physics*, *124*(11), 8319–8351. https://doi.org/10.1029/2018JA025940

Li, W., Ma, Q., Thorne, R. M., Bortnik, J., Kletzing, C. A., Kurth, W. S., et al. (2015). Statistical properties of plasmaspheric hiss derived from Van Allen Probes data and their effects on radiation belt electron dynamics. *Journal of Geophysical Research: Space Physics*, *120*(5), 3393–3405. https://doi.org/10.1002/2015JA021048

Li, W., Ma, Q., Thorne, R. M., Bortnik, J., Zhang, X. J., Li, J., et al. (2016). Radiation belt electron acceleration during the 17 March 2015 geomagnetic storm: Observations and simulations. *Journal of Geophysical Research: Space Physics*, *121*(6), 5520–5536. https://doi.org/10.1002/2016JA022400

Li, W., Shen, X.-C., Ma, Q., Capannolo, L., Shi, R., Redmon, R. J., et al. (2019). Quantification of energetic Electron precipitation driven by plume whistler mode waves, Plasmaspheric hiss, and exohiss. *Geophysical Research Letters*, *46*(7), 3615–3624. https://doi.org/10.1029/2019GL082095

Lyons, L. R., & Thorne, R. M. (1973). Equilibrium structure of radiation belt electrons. *Journal of Geophysical Research*, *78*(13), 2142–2149. https://doi.org/10.1029/ja078i013p02142

Ma, Q., Li, W., Bortnik, J., Thorne, R. M., Chu, X., Ozeke, L. G., et al. (2018). Quantitative evaluation of radial diffusion and local acceleration processes during GEM challenge events. *Journal of Geophysical Research: Space Physics*, *123*(3), 1938–1952. https://doi.org/10.1002/2017JA025114

Ma, Q., Li, W., Thorne, R. M., Bortnik, J., Reeves, G. D., Kletzing, C. A., et al. (2016). Characteristic energy range of electron scattering due to plasmaspheric hiss. *Journal of Geophysical Research: Space Physics*, *121*(12), 11737–11749. https://doi.org/10.1002/2016JA023311

Ma, Q., Li, W., Thorne, R. M., Ni, B., Kletzing, C. A., Kurth, W. S., et al. (2015). Modeling inward diffusion and slow decay of energetic electrons in the Earth's outer radiation belt. *Geophysical Research Letters*, *42*(4), 987–995. https://doi.org/10.1002/2014GL062977

Ma, Q., Li, W., Zhang, X.-J., Bortnik, J., ShenBoyd, X. A. J., Kurth, W. S., et al. (2021). Global survey of electron precipitation due to hiss waves in the Earth's plasmasphere and plumes. *Journal of Geophysical Research: Space Physics*, *126*(8), e2021JA029644. https://doi.org/10.1029/2021JA029644

Mauk, B. H., Fox, N. J., Kanekal, S. G., Kessel, R. L., Sibeck, D. G., & Ukhorskiy, A. (2013). Science objectives and rationale for the radiation belt storm Probes mission. *Space Science Reviews*, *179*(1–4), 3–27. https://doi.org/10.1007/s11214-012-9908-y

Meredith, N. P., Horne, R. B., Thorne, R. M., & Anderson, R. R. (2009). Survey of upper band chorus and ECH waves: Implications for the diffuse aurora. *Journal of Geophysical Research*, *114*(A7), A07218. https://doi.org/10.1029/2009JA014230

Morley, S. K. (2020). Challenges and opportunities in magnetospheric space weather prediction. *Space Weather*, *18*(3), e2018SW002108. https://doi.org/10.1029/2018SW002108

Morley, S. K., Sullivan, J. P., Henderson, M. G., Blake, J. B., & Baker, D. N. (2016). The Global Positioning System constellation as a space weather monitor: Comparison of electron measurements with Van Allen Probes data. *Space Weather*, *14*(2), 76–92. https://doi.org/10.1002/2015SW001339

Mourenas, D., & Ripoll, J.-F. (2012). Analytical estimates of quasi-linear diffusion coefficients and electron lifetimes in the inner radiation belt. *Journal of Geophysical Research*, *117*(A1), A01204. https://doi.org/10.1029/2011JA016985

Murray, S. A. (2018). The importance of ensemble techniques for operational space weather forecasting. *Space Weather*, *16*(7), 777–783. https://doi.org/10.1029/2018SW001861

Myagkova, I. N., Shugai, Y. S., Kalegaev, V. V., Kolmogorova, V. A., & Dolenko, S. A. (2020). Medium-term prediction of relativistic electron fluxes in a geostationary orbit using machine learning methods based on observations of solar coronal holes. *Geomagnetism and Aeronomy*, *60*(3), 279–288. https://doi.org/10.1134/S0016793220030123

Ni, B., Bortnik, J., Thorne, R. M., Ma, Q., & Chen, L. (2013). Resonant scattering and resultant pitch angle evolution of relativistic electrons by plasmaspheric hiss. *Journal of Geophysical Research: Space Physics*, *118*(12), 7740–7751. https://doi.org/10.1002/2013JA019260

Ni, B., Hua, M., Zhou, R., Yi, J., & Fu, S. (2017). Competition between outer zone electron scattering by plasmaspheric hiss and magnetosonic waves. *Geophysical Research Letters*, *44*(8), 3465–3474. https://doi.org/10.1002/2017GL072989

Ni, B., Thorne, R. M., Shprits, Y. Y., & Bortnik, J. (2008). Resonant scattering of plasma sheet electrons by whistler-mode chorus: Contribution to diffuse auroral precipitation. *Geophysical Research Letters*, *35*(11), L11106. https://doi.org/10.1029/2008GL034032

O'Brien, T. P., Claudepierre, S. G., Guild, T. B., Fennell, J. F., Turner, D. L., Blake, J. B., et al. (2016). Inner zone and slot electron radial diffusion revisited. *Geophysical Research Letters*, *43*(14), 7301–7310. https://doi.org/10.1002/2016GL069749

Ozhogin, P., Tu, J., Song, P., & Reinisch, B. W. (2012). Field-aligned distribution of the plasmaspheric electron density: An empirical model derived from the IMAGE RPI measurements. *Journal of Geophysical Research*, *117*(A6), A06225. https://doi.org/10.1029/2011JA017330

Pires de Lima, R., Chen, Y., & Lin, Y. (2020). Forecasting megaelectron-volt electrons inside earth's outer radiation belt: PreMevE 2.0 based on supervised machine learning algorithms. *Space Weather*, *18*(2), e2019SW002399. https://doi.org/10.1029/2019SW002399

Reeves, G. D., Chen, Y., Cunningham, G. S., Friedel, R. W. H., Henderson, M. G., Jordanova, V. K., et al. (2012). Dynamic radiation environment assimilation model: Dream. *Space Weather*, *10*(3), S03006. https://doi.org/10.1029/2011sw000729

Saikin, A. A., Shprits, Y. Y., Drozdov, A. Y., Landis, D. A., Zhelavskaya, I. S., & Cervantes, S. (2021). *Reconstruction of the Radiation Belts for Solar Cycles 17–24 (1933–2017)* (Vol. 19). Space Weather. https://doi.org/10.1029/2020SW002524

Sarma, R., Chandorkar, M., Zhelavskaya, I., Shprits, Y., Drozdov, A., & Camporeale, E. (2020). Bayesian inference of quasi-linear radial diffusion parameters using Van Allen Probes. *Journal of Geophysical Research: Space Physics*, *125*(5), e2019JA027618. https://doi.org/10.1029/2019JA027618

Schulz, M., & Lanzerotti, L. J. (1974). Particle diffusion in the radiation belts. *Physics and Chemistry in Space*. (Vol. 7). Springer.

Sheeley, B. W., Moldwin, M. B., Rassoul, H. K., & Anderson, R. R. (2001). An empirical plasmasphere and trough density model: CRRES observations. *Journal of Geophysical Research*, *106*(A11), 25631–25641. https://doi.org/10.1029/2000JA000286

Shprits, Y., Kellerman, A., Kondrashov, D., & Subbotin, D. (2013). Application of a new data operator-splitting data assimilation technique to the 3-D VERB diffusion code and CRRES measurements. *Geophysical Research Letters*, *40*(19), 4998–5002. https://doi.org/10.1002/grl.50969

Shprits, Y. Y., Subbotin, D. A., Meredith, N. P., & Elkington, S. R. (2008). Review of modeling of losses and sources of relativistic electrons in the outer radiation belt II: Local acceleration and loss. *Journal of Atmospheric and Solar-Terrestrial Physics*, *70*(14), 1694–1713. https://doi.org/10.1016/j.jastp.2008.06.014

Smirnov, A. G., Berrendorf, M., Shprits, Y. Y., Kronberg, E. A., Allison, H. J., Aseev, N. A., et al. (2020). Medium energy electron flux in earth's outer radiation belt (merlin): A machine learning model. *Space Weather*, *18*(11), e2020SW002532. https://doi.org/10.1029/2020SW002532

Spence, H. E., Reeves, G. D., Baker, D. N., Blake, J. B., Bolton, M., Bourdarie, S., et al. (2013). Science goals and overview of the energetic particle, composition, and thermal plasma (ECT) suite on NASA's radiation belt storm Probes (RBSP) mission. *Space Science Reviews*, *179*(1-4), 311–336. https://doi.org/10.1007/s11214-013-0007-5

Subbotin, D. A., & Shprits, Y. Y. (2009). Three-dimensional modeling of the radiation belts using the Versatile Electron Radiation Belt (VERB) code. *Space Weather*, *7*(10), S10001. https://doi.org/10.1029/2008sw000452

Thorne, R. M. (2010). Radiation belt dynamics: The importance of wave-particle interactions. *Geophysical Research Letters*, *37*(22), L22107. https://doi.org/10.1029/2010gl044990

Thorne, R. M., Li, W., Ni, B., Ma, Q., Bortnik, J., Baker, D. N., et al. (2013a). Evolution and slow decay of an unusual narrow ring of relativistic electrons near L ∼ 3.2 following the September 2012 magnetic storm. *Geophysical Research Letters*, *40*(14), 3507–3511. https://doi.org/10.1002/grl.50627

Thorne, R. M., Li, W., Ni, B., Ma, Q., Bortnik, J., Chen, L., et al. (2013b). Rapid local acceleration of relativistic radiation-belt electrons by magnetospheric chorus. *Nature*, *504*(7480), 411–414. https://doi.org/10.1038/nature12889

Tsurutani, B. T., Park, S. A., Falkowski, B. J., Lakhina, G. S., Pickett, J. S., Bortnik, J., et al. (2018). Plasmaspheric hiss: Coherent and intense. *Journal of Geophysical Research: Space Physics*, *123*(12), 10009–10029. https://doi.org/10.1029/2018JA025975

Tsyganenko, N. A., & Sitnov, M. I. (2005). Modeling the dynamics of the inner magnetosphere during strong geomagnetic storms. *Journal of Geophysical Research*, *110*(A3), A03208. https://doi.org/10.1029/2004JA010798

Tu, W., Cunningham, G. S., Chen, Y., Henderson, M. G., Camporeale, E., & Reeves, G. D. (2013). Modeling radiation belt electron dynamics during GEM challenge intervals with the DREAM3D diffusion model. *Journal of Geophysical Research: Space Physics*, *118*(10), 6197–6211. https://doi.org/10.1002/jgra.50560

Tu, W., Cunningham, G. S., Chen, Y., Morley, S. K., Reeves, G. D., Blake, J. B., et al. (2014). Event-specific chorus wave and electron seed population models in DREAM3D using the Van Allen Probes. *Geophysical Research Letters*, *41*(5), 1359–1366. https://doi.org/10.1002/2013GL058819

Xiao, F., Su, Z., Zheng, H., & Wang, S. (2009). Modeling of outer radiation belt electrons by multidimensional diffusion process. *Journal of Geophysical Research*, *114*(A3), A03201. https://doi.org/10.1029/2008JA013580

Zhang, S., Rae, I. J., Watt, C. E. J., Degeling, A. W., Tian, A., Shi, Q., et al. (2021). Determining the temporal and spatial coherence of plasmaspheric hiss waves in the magnetosphere. *Journal of Geophysical Research: Space Physics*, *126*(2), e2020JA028635. https://doi.org/10.1029/2020JA028635

Zhao, H., Ni, B., Li, X., Baker, D. N., Johnston, W. R., Zhang, W., et al. (2019). Plasmaspheric hiss waves generate a reversed energy spectrum of radiation belt electrons. *Nature Physics*, *15*(4), 367–372. https://doi.org/10.1038/s41567-018-0391-6

References From the Supporting Information

Glauert, S. A., & Horne, R. B. (2005). Calculation of pitch angle and energy diffusion coefficients with the PADIE code. *Journal of Geophysical Research*, *110*(A4), A04206. https://doi.org/10.1029/2004JA010851